Element Identification by K-Edge Imaging Using Spectroscopic Photon Counting Detectors

Michael K. Schütz, Julian Fey, Simon Procz, Juan S. Useche, Gerardo Roque, and Michael Fiederle

***Abstract*— The reliable identification of multiple elements in a single X-ray exposure is advantageous in various fields of interest like medicine, nondestructive materials research, homeland security, waste management, and the mining industry. Elements of interest can be identified by analyzing how an X-ray transmission spectrum correlates with the element's K-edge. Timepix3 (TPX3)-based photon-counting detectors offer the possibility of spectroscopic X-ray imaging, allowing to record the changes in the transmission spectrum and, consequently, for element identification. This article presents element identification using a single X-ray image recorded with a 2 mm CdZnTe TPX3 detector. The analysis is based on the K-edge method, analyzing sharp edges in the absorption spectrum of an exposed object. The work describes the follow-up investigation of a material discrimination study utilizing several discrete energy thresholds. Single layers of 200 μm thick foils of different metals have been investigated as elements of interest. No overlaying elements or composites have been used in the absorption phantom. The method shown is limited to a specific absorption ratio inside the element, which means the influence of the absorber on the spectrum measured must result in a recognizable K-edge. Within this work, it is possible to identify eight out of nine different elements of the absorption phantom with K-edges distributed over an energy spectrum from 8 to 70 keV.**

***Index Terms*— CdZnTe detectors, K-edge imaging, Medipix, nondestructive testing, photon counting detectors (PCDs), semiconductor detectors, spectroscopic X-ray imaging, Timepix, waste recovery, X-ray detectors.**

I. Introduction

MATERIAL identification with X-ray imaging is of great interest in nondestructive materials research, homeland security [1], [2], the mining industry [3], and the waste management industry [4], [5]. Traditional X-ray imaging techniques only allow separating areas with high and low radiation absorption. The absorption of the initial radiation source depends on material-specific properties of the absorber and its thickness. These properties include the density of the material and its absorption coefficient. Since the absorption coefficient depends on the energy of the absorbing X-rays, it can be used as an identifier for a material or a specific element.

Manuscript received 15 May 2023; revised 1 September 2023 and 9 November 2023; accepted 15 November 2023. Date of publication 23 November 2023; date of current version 19 January 2024. This work was supported by BMBF under Grant 02NUK070A. *(Corresponding author: Michael K. Schütz.)*

The authors are with the Freiburg Materials Research Center (FMF), Albert-Ludwigs-University Freiburg, Freiburg im Breisgau, 79104 Baden-Württemberg, Germany (e-mail: michael.schuetz@fmf.uni-freiburg.de).

Color versions of one or more figures in this article are available at https://doi.org/10.1109/TNS.2023.3336458.

Digital Object Identifier 10.1109/TNS.2023.3336458

The approach of using different energy ranges to distinguish materials in one X-ray image was already presented in 1976. Alvarez and Macovski [6] suggested that utilizing the information of the energy-depending X-ray image could be useful in medical applications. The dual energy method requires recording two images of the same object at two different energies. A thickness-independent absorption relation r can be found by inverting the Beer–Lambert Law for the absorption coefficient μ. The calculation of the ratio of the absorption coefficients can be derived from the measurement at low radiation energy μ_l and the one measured at high radiation energy μ_h. μ_l and μ_h are determined by taking the logarithm of the fraction of the recorded transmission intensity I and the recorded intensities without absorber I_0. The factor r is material specific and can be used as identifier as follows:

$$r = \frac{\mu_h}{\mu_l} = \ln\left(\frac{I_h}{I_{h0}}\right) / \ln\left(\frac{I_l}{I_{l0}}\right). \tag{1}$$

Lehman et al. [7] as well as Hughes et al. [8] proved the functionality of this theoretical approach by successfully differentiating materials in radiographs. Since then, dual-energy X-ray imaging and CT applications have been widely available and are used in several fields. Currently, material identification is mainly performed using the dual energy approach. The principle of the dual-energy approach is to record two separate X-ray images at different X-ray energies. This can be achieved either by adjusting the acceleration voltage of the X-ray source between two recordings and taking one X-ray image for each acceleration voltage, or by recording a broad energy spectrum with a sandwiched detector array consisting of two or more consecutive detectors. The detectors are typically sensitive to different energy ranges, and additional filters such as copper are commonly placed between the detectors. By comparing the absorption of objects of interest across these different energy regions, material-specific properties can be derived, allowing for the separation of materials.

Novikov et al. [9] investigated material identification with a dual-energy approach in the Compton scattering dominant energy range from 1 to 10 MeV. They achieved material identification with a precision of the atomic number $Z_{\text{meas}} = Z_{\text{real}} \pm 10$, regardless of object thickness.

A new possibility of measurement is given by the availability of photon counting detectors (PCDs). PCDs allow recording a broad energy spectrum by creating specific energy windows with various thresholds or can be fully spectroscopic, recording the energy per event for further energy binning. This energy information allows us to differentiate and identify

materials or chemical elements. Vavrik and Jakubek [10] showed that a PCD with two different energy thresholds could be used to apply K-edge imaging and successfully differentiate various materials in a single radiograph. It was possible to highlight a specific material in an X-ray image by using different energy thresholds and comparing the resulting images. For these recordings, a Medipix2 detector was used [11]. Rinkel et al. [12] used a PCD with a CdTe sensor to investigate the improvement of material identification by varying the number of energy thresholds. They investigated different materials in the energy range from 22 to 130 keV and found that material identification reliability increases with the number of thresholds. Moreover, they found that threshold optimization is no longer needed with a fully spectroscopic detector.

Other ways exist to identify materials with appropriate calibration methods. Uher et al. [13] showed that a signal-to-thickness calibration method makes material separation with a silicon-based Medipix2 PCD possible. In this technique, materials can be identified by comparing the absorption with the attenuation of various thicknesses of aluminum in different energy ranges. Beldjoudi et al. [14] also proposed a new method for material decomposition in CT and X-ray images. They developed an optimization routine for the PCD energy bins and stated that a fully spectroscopic working detector was most suitable for material identification, since no threshold optimization is required. Brambilla et al. [15] also developed a novel method of material analysis that relied on base materials. Comparing recordings of an object of interest with a previously recorded calibration dataset, they distinguished and identified the effective atomic number of PE and PVC samples, regardless of thickness. They stated that additional effects must be considered for reliable material identification using a broad energy spectrum radiation source instead of a monochromatic energy beam.

Recent material identification and separations mainly focus on CT applications, in which material overlap is commonplace, and more sample details are available than in a 2-D radiograph. This work deals exclusively with material identification in radiographs. Work dealing solely with CT will not be discussed in further detail. Further information can be found in the literature [16], [17], [18], [19], [20], [21], [22], [23].

As mentioned above, the dual energy approach and the developed extensions allow the differentiation and identification of materials in a suitable energy range where no material K-edges are present. However, the K-edge of a material is a very prominent and specific indicator of the absorber's chemical element. Applying PCDs with suitable energy thresholds around the K-edges of materials of interest uses it as an advantage. Pani et al. [24] showed in 2012 that K-edge imaging can benefit from measuring with PCDs. They compared two images in different energy ranges, one picture taken below, and one above, the K-edge of an absorber material. They removed the background more efficiently, resulting in higher contrast and lower noise than charge-integrating devices. Ballabriga et al. [25] showed that by taking advantage of the material's K-edges by using suitable energy thresholds and comparing the resulting images it is possible to differentiate four materials that previously were not distinguishable in a traditional grayscale radiograph. Schütz et al. [26] showed that by using the same detector model, a Medipix3 [25] PCD with eight energy thresholds, K-edge absorption could be used to differentiate and separate up to eight materials in one single X-ray recording.

This work investigates the possibility of material identification by the analysis of the transmission energy spectrum using an absorption phantom consisting of nine metal foils. The differences between the initial and the transmission X-ray spectra give the possibility to identify the different chemical elements. The detector used is a Timepix3 (TPX3) detector [27] coupled to a Cadmium–Zinc–Telluride (CdZnTe) sensor. Beyond pure material separation, this work focuses on identifying previously unknown elements using the K-edges. The novelty of this approach is the analysis of the absorber's chemical element in combination with an imaging technique. The chemical elements can be directly determined from the X-ray spectrum. The focus of this work is on the feasibility analysis of the concept rather than demonstrating a practical real-world application.

II. Theory

A. Photon Interaction and K-Edge

The Beer-Lambert law describes the intensity change of an initial radiation source due to interactions of the photons in an absorbing element (1). It models the total decrease in radiation intensity due to interactions of the photons with the absorber of a well-defined thickness

$$I(E) = I_0(E) \cdot \exp[-\mu(E) \cdot d]. \tag{2}$$

$\mu(E)$ is the energy-dependent absorption coefficient, $I_0(E)$ is the incident intensity of the radiation source, and $I(E)$ is the resulting intensity after the photons travel along the thickness d of the element.

X-ray photons can interact with matter through different interaction processes during exposure. The interactions in the energy range between 0 and 100 keV are the Rayleigh scattering, the Compton scattering, and the Photoelectric effect. The probability that a photon undergoes a scatter interaction is relatively steady over a wide range of energies. The Photoelectric effect is only possible if the incoming photon's energy exceeds the binding energy of an atom's electron. Furthermore, the probability of interacting through photo-effect is more likely than the scattering interactions for energies above the binding energy in the energy range between 0 and 100 keV.

For a particular set of elements, the inner-most orbital electron binding energy lies in the already mentioned energy range. Consequently, the probability of photon absorption increases considerably. This higher absorption probability leads to a substantial reduction of transmitted photons above that energy, forming a local maximum in the absorption spectrum known as an element-specific K-edge. The K-edge can be used to identify the underlying element because each element's electron K-shell binding energy is unique.

III. Measurements and Methods Used

The measurements are divided into the premeasurements for the detector equalization as well as calibration and the main

measures for the final element identification. All measurements were recorded with a TPX3 detector using a CdZnTe sensor. A continuous energy spectrum from an X-ray tube with Tungsten (W) target at 100 kVp, was used for all measurements. In Sections III-A–III-C, the components of the measurement setup are described in detail.

A. TPX3 Detector

A TPX3 ASIC flip chip bonded with a 2 mm thick CdZnTe sensor was used as a detector. The TPX3 detector unit is a hybrid photon-counting semiconductor detector developed by the Medipix3 collaboration at CERN [28]. It is produced in 130 nm CMOS technology with 256 × 256 pixels and a pixel pitch of 55 μm. The active detector area is 1.98 cm^2. Further details about the TPX3 detector design, hardware components, and its readout hardware configuration are described in [27].

While the TPX3 detector offers different modes of operation, only the data-driven readout mode has been used in this work. In this mode, the position, the time of arrival (ToA), and the duration that the induced signal exceeds the detector's energy threshold are recorded for each event. This duration is called the time over threshold (ToT) value, and measures the energy of the interactions in clock pulses. The ToT is directly proportional to the energy of the registered photon and can be used to calculate the X-ray energy with proper calibration [29], [30]. The energy response functions of the individual pixels assign the measured raw ToT values to calibrated energy in keV.

The time resolution of the TPX3 detector is 1.562 ns. The adjustable energy threshold used in this work was set to 6 keV to avoid false-positive events resulting from noise in the detector electronics overcoming it. The energy information is obtained in discretized form since the photon's energy is calculated from the number of collected charge and the discrete clock pulses. The registered events need to be clustered after the measurements due to the effect of charge sharing. This gives the possibility to restore the original photon energy, the total absorption spectrum, and the position of interaction. Charge sharing occurs when multiple neighboring pixels share the charge of a single event, causing spectral distortions of the uncorrected data. The charge-sharing effect and the clustering advantages are described in detail in [31] and [32]. The energy resolution of the detector used was assessed to have a full width at half maximum (FWHM) of 7.13 keV at 60 keV. Additional details on the detector's performance can be found in a previous study using the same detector [33].

B. Absorption Phantom

An absorption phantom was built with elements covering different requirements depending on the field of possible application. It consists of nine 5 × 5 mm^2 metallic foils, each 200 μm thick. The complete list of chosen elements is shown in Table I. The metals have been selected by their K-edge energies covering a wide energy range from 8.99 to 69.52 keV. Additionally, two contrast agents Gadolinium (Gd) and Iodine (I), were included which are used in typically medical imaging. Tungsten (W) was also included since it is in good comparison to the K-edge energy of Gold (Au), which is also used as a contrast agent [34]. To investigate the limits of element separation with K-edges close to each other, Molybdenum (Mo), Zirconium (Zr), and Niobium (Nb) were incorporated, as well as Neodymium (Nd) and Tin (Sn). Finally, Copper (Cu) was added to measure identification capabilities for low-Z elements.

TABLE I
ELEMENTS AND PROPERTIES OF THE ABSORPTION PHANTOM

Element	Symbol	Atomic Number	Density [g/cm^3]	K-edge Energy [keV]
Copper	Cu	29	8.96	8.993
Zirconium	Zr	40	6.51	17.997
Niobium	Nb	41	8.75	18.985
Molybdenum	Mo	42	10.22	20.002
Tin	Sn	50	7.31	29.211
Iodine	I	53	4.94	33.168
Neodymium	Nd	60	6.8	43.538
Gadolinium	Gd	64	7.9	50.207
Tungsten	W	74	19.3	69.517

The chemical elements used in the absorption phantom with their relevant properties. All values have been taken from [43]

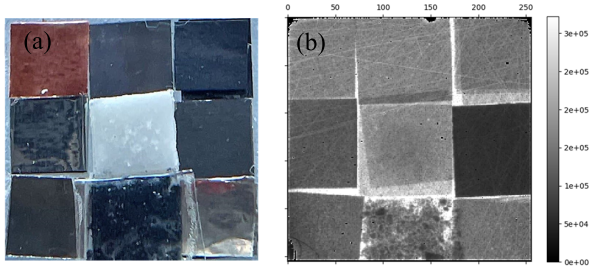

Fig. 1. (a) Photograph and (b) X-ray image of the absorption phantom produced. The scale shows the number of recorded photons per pixel.

Unlike the other materials, the I and Nd parts did not consist of 200 μm thick foils. For I, an Iodine -based contrast agent, Imeron [35], was dissolved in water with a ratio of 1:1 water and iodine, respectively. The solution was dried on filter paper, with the remains forming a crystalline structure. The Nd region was created by pulverizing Nd magnets and fixing the powder by an adhesive tape to create an area comparable to the selected foils. All nine elements were placed on a 4 μm thick PMMA foil, functioning as a supporting structure. A photograph and an X-ray image of the absorption phantom are shown in Fig. 1.

C. Detector Calibration and Experimental Setup

The measurements were performed with a horizontally aligned setup, shown in Fig. 2. A Hamamatsu L10711 X-ray tube was used as a radiation source. It was operated with a W target at 100 kVp for calibration and final measurements to stimulate all the absorption phantom's K-edges.

All preliminary measurements were performed using the setup shown in Fig. 2(a). The TPX3 threshold equalization was done by applying the noise edge technique described in [36], which is implemented in the detector readout software. The pixel-wise energy calibration was done by recording the fluorescence radiation of several elements [30]. By relating the

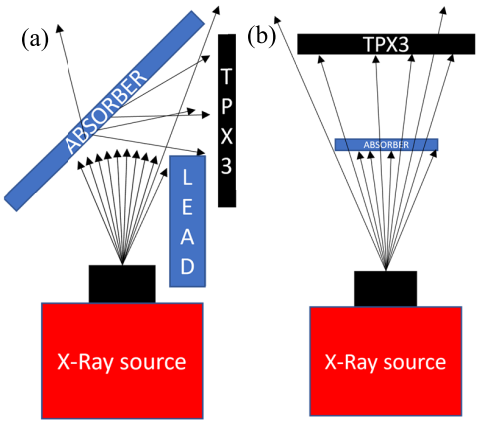

Fig. 2. Experimental setups for (a) calibration and (b) main measurements. (a) TPX3 detector is placed outside the radiation direction, and shielded, collecting mainly fluorescence photons. (b) TPX3 detector is placed behind the absorber in the radiation direction.

intensity-weighted mean energy of the K_α and K_β fluorescence lines with the mean value of the measured energy peaks, it was possible to create a calibration curve for each pixel. The detector was shielded with 5 cm of Lead (Pb) against photons of the primary beam. The fluorescing probes were placed on the central emission axis, tilted by 45° with respect to the detector plane, ensuring the highest cross section for both the detector and the fluorescent sources. The technique and the determination of the energy response function are described in detail in [29], [37], and [38].

The main measurements were performed using the setup shown in Fig. 2(b). The TPX3 detector and the absorption phantom were placed centrally in the main-emission axis. The distance between the absorption phantom and the sensor was 5 mm. The total acquisition time was defined by the minimum average intensity of 6×10^4 counts per pixel for the region with the highest absorption to obtain a usable spectrum in every pixel. The region with the highest absorption was expected to be the region with W. The mean count rate of the total detector was 1.4×10^6 counts/pixel. This requirement should provide enough photons in each pixel to ensure that the transmission spectrum is represented realistically. The X-ray spectrum was filtered with 5 mm PMMA to reduce the number of low energy photons, which do not contribute information on the K-edges but increase the total recorded data.

D. K-Edge Method

The complete absorption spectrum can be described by the total spectrum intensity (I_{tot}) divided into a sum of the individual energy channel intensities over all energy channels available as follows:

$$I_{\text{tot}} = \sum_{i=0}^{E\_\text{max}} I_i = \sum_{i=0}^{E\_\text{max}} I_{0i} * \exp[-\mu_i d]. \tag{3}$$

The energy-dependent absorption coefficient can be calculated on a per-channel basis using the binned energy spectrum of the X-ray tube without an absorber ($S_{\text{FF}-i}$) as the original intensity $I_{0i}(E)$ and the spectrum recorded with an absorber ($S_{\text{RA}-i}$) as the resulting intensity $I_i(E)$. The absorber thickness is represented in d. By rearranging the individual channel terms in (3), (4) is formed. It represents the measured attenuation coefficient

$$\mu(E) = -\frac{\ln\left[\frac{I(E)}{I_0(E)}\right]}{d}. \tag{4}$$

By taking its discrete derivative, the maximum change in absorption concerning energy and, therefore, the K-edge position of the absorption spectrum can be determined. If the interaction by the photo-effect is the most significant influence on the absorption spectrum, the expected location of the K-edge is located at the maximum of derivative pointing directly to the underlying absorption element

$$\mu'(E) = \frac{d}{dE}\left(-\ln\left[\frac{I(E)}{I_0(E)}\right] \cdot \frac{1}{d}\right) = \frac{d}{dE}\left(-\ln\left[\frac{I(E)}{I_0(E)}\right]\right) \cdot \frac{1}{d}. \tag{5}$$

Applying this technique, the elements of interest can be directly determined by their measured spectra in a single X-ray radiograph.

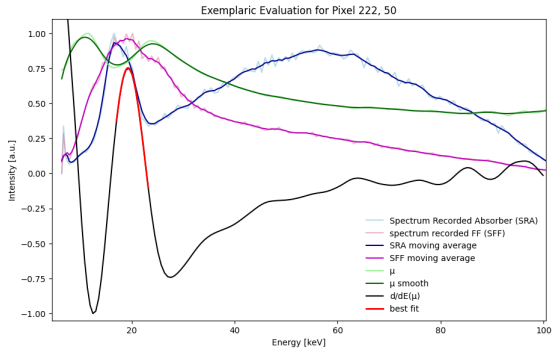

Fig. 3. Evaluation method for determining the K-edge of the measured spectrum. The spectrum behind the absorber SRA (blue) is compared to the spectrum without absorber SFF (purple), combining with (4) to the absorption factor (green). By fitting the most prominent local maxima of the derivative of $\mu(E)$, the K-edge is determined by the mean value of the Gaussian fit. The curves of SRA, SFF, and $\mu(E)$ were scaled to improve the visibility on the graph.

IV. Measured Data, Analysis, and Results

The total absorption phantom was recorded in a single X-ray exposure using the setup described in Section III-C. The measurements were preprocessed by clustering the data and masking noisy pixels. Afterward, each pixel spectrum was analyzed individually. An example is shown in Fig. 3 for one Mo-covered pixel.

The purple curve shows the moving average of the original energy spectrum of the source S_{FF} as measured by the TPX3 pixel of the detector. The blue curve represents the moving average of the absorption spectrum recorded by the same specific pixel S_{RA}. The green curve represents the absorption coefficient $\mu(E)$ calculated from S_{RA} and S_{FF} using (4). The gray curve is the discrete derivative of the resulting absorption coefficients per energy $\mu(E_i)$.

The thickness of the absorber contributes to the weighted absorption function as an energy-independent scaling and has no direct influence on the K-edge determination. The thickness plays a role regarding detectability of the changes in the transmission spectrum. The algorithm of the element identification is designed for each pixel to assign the element with the

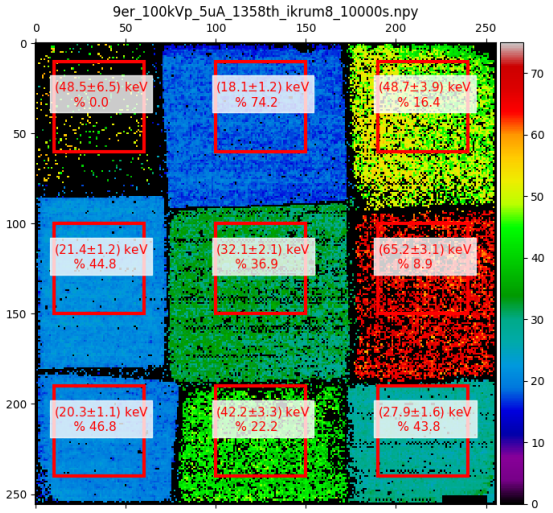

Fig. 4. Identified K-edge energies of the absorption phantom radiograph. The different materials are well distinguishable, and the mean values are in good agreement with the literature values. The number of pixels within the marked area, whose determined K-edge energy corresponds to the literature values within the standard deviation of the marked area, is expressed as a percentage.

most significant influence on the transmission spectrum of the pixel. Consequently, only one chemical element can be detected per pixel, regardless of the actual elements present. The identification of an element assigned to the pixel is carried out according to the following scheme: the most prominent local maximum of the weighted absorption function was taken as the starting point to find the K-edge value; this maximum was fit with a Gaussian distribution; the mean value of this Gaussian was taken as the responding energy. The found K-edge value was then assigned to the pixel as the dominating value, creating an image based on the reconstructed K-edge values only, as shown in Fig. 4. In the case of Fig. 3, the maximum change in absorption is located at 19.3 keV, which corresponds to the K-edge of Mo.

False-positive assignments can occur since the algorithm is forced to assign each pixel a K-edge value within three tries of fitting the derivative. The assumed K-edge is accepted if the relative amplitude of the corresponding Gaussian fit converges, and the mean value lies in the energy range between 6 and 75 keV. A second criterion is defined if the standard deviation of this Gaussian function lies between 2 and 10. Additionally, the values were filtered by comparison with a 9×9 neighborhood around the pixel. The assigned value was accepted if the current pixel value differed a maximum of five from the average value of the surroundings. All pixels not fitting the quality criteria were masked and shown as black in Fig. 4 and were not included in the final evaluation.

As the final evaluation for each region in Fig. 4, the mean of the assigned values inside the drawn rectangles was calculated, representing the mean values of the found K-edge energies. The given uncertainties are the standard deviations from those regions. The literature values of the K-edge energies used in this work can be found on NIST [39] The number of pixels within the marked area, whose determined K-edge energy corresponds to the literature values within the standard deviation of the marked area, is expressed as a percentage.

Eight elements could be identified reliably for a total of nine. The mean values of the K-edges in these areas coincide with the literature values by the standard deviation of these areas. Cu could not be identified because of the low energy level of the related K-edge compared to the noise. Additionally, the energy threshold was set close to the K-edge of Cu, worsening the detectability further since a rise in absorption is not detectable over only three energy bins. As a result, pixels in the Cu area were assigned to random local maxima of the derivative of the absorption coefficient μ.

TABLE II
RESULTS OF THE SECOND MEASUREMENT

	Mean Counts	4E+02	1E+03	3E+03	1E+04	3E+04	4E+04
	thickness [µm]	% corr	% corr	% corr	% corr	% corr	% corr
Sn	30	13.3	39.3	48.3	68.3	68.3	66.5
	20	0.5	20.8	40.5	59.0	66.0	63.8
	10	0.0	0.0	5.3	23.5	28.5	31.5
Nb	30	18.4	50.8	76.3	81.8	83.9	86.8
	20	2.6	50.6	69.0	69.3	69.3	72.0
	10	0.0	0.0	0.5	24.3	28.4	26.3
Zr	30	35.6	67.2	82.4	90.0	90.1	90.3
	20	0.0	0.0	40.3	50.3	52.5	53.4
	10	0.0	0.0	0.0	0.0	0.0	0.0

The relative number of correct assigned pixels in each area of the phantom. The percentage of the correct assigned pixels correspond to the absorber thickness and the total number of counts.

A second series of measurements was carried out to investigate qualitatively the various influences on the K-edge values to improve the identification of elements based on the spectrum. This analysis was focused on the influence of varying absorber thickness and different numbers of total counts on the detectability of the K-edges. Therefore, a part of the absorption phantom was examined, which was already investigated in a previous study [26]. The area under investigation consisted of three different elements (Sn, Nb, Zr) with three different absorber thicknesses, 10, 20, and 30 μm, respectively. This phantom was recorded for various durations. The impact of the resulting total measured count rate was correlated to the absorber thickness by examining the number of accurately detected pixels across different time frames. The result of the analysis is shown in Table II. More pixels can be correctly assigned in an area if the absorber is thicker.

The thickness has a more significant influence on the transmission spectrum. More pixels are assigned correctly as expected, if the measurement is based on higher statistics, i.e., the actual spectrum can be recorded with fewer fluctuations.

An evaluation of this phantom is shown in Fig. 5. Furthermore, it can be seen that the presented method utilizing the full energy spectrum, is superior to a simple energy threshold subtraction as it was performed in previous studies. Earlier methods permitted a rough distinction of elements by their absorption within different energy channels. However, these methods lacked reliability and failed to identify specific chemical elements. Adjustments were made to the energy thresholds to better detect the K-edges we were targeting. The findings of this study have shown that it is now possible to identify unknown elements with pixel-level accuracy.

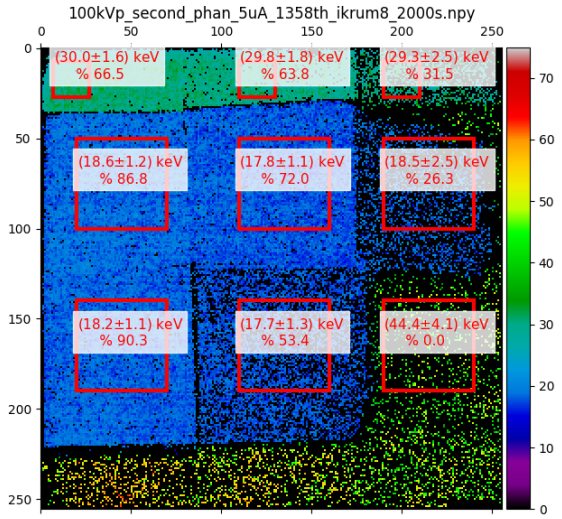

Fig. 5. Exemplary result of the second absorption phantom. The thickness of the metal foils decreases from left to right from 30 to 10 μm.

V. Conclusion and Discussion

The element identification of single sheets of elements is possible by directly analyzing the absorption spectrum of several elements. The method described does not require calibration measurements with reference elements to create a detector-specific database. A simple energy calibration of the sensor is sufficient for reliable results. Furthermore, the absorber's chemical element can be determined with pixel accuracy and offers the potential to refine the spatial element determination by further analysis techniques such as subpixel resolution. However, this technique has some limitations. The absorber thickness is a compromise between efficiency and sensitivity: it must be sufficiently thick to generate an influence on the spectrum but not too thick to reduce the intensity in the energy range of interest. Related to the previous point, the number of photons registered per energy channel should be in general a smooth energy spectrum. Otherwise, the differences in neighboring energy channels will lead to fluctuations in the absorption-factor derivative and subsequently to false-positive K-edge identifications. The suitable absorber thickness depends on the spectrum's initial intensity, which can be tuned toward a better detection result.

Identifying elements, e.g., Cu with a K-edge energy close to the lower energy threshold is challenging. The number of photons per energy channel in the areas of the boundaries of the spectrum leads to disturbance in the derivation of the absorption coefficient curve and, consequently, to falsely identified pixels. The most reliably recognized elements were those with K-Edges distributed in the energy range with the highest initial intensity between 10 and 40 keV. Therefore, the Mo, Zr, Nb, Sn, and I regions had the highest percentages of correct assignment. This result is in good agreement with the previous study [26], where these elements were also most differentiable from the others using a comparable energy spectrum. The strong correlation between successful material identification and the number of registered photons was confirmed by a second measurement series.

In the Cu and W regions, fewer pixels could be assigned correctly compared to other areas, which is in agreement with the presented theory. In both cases, the statistics of counted photons were insufficient to identify a K-Edge reliably. The low energy threshold of 6 keV is not suitable for the Cu K-Edge identification. due to the low energy of 8.9 keV. The number of energy bins below the energy threshold was too small to recognize a K-edge reliably. Assigned values are compared with the values of the neighboring pixels and sorted out if the values differ more than two standard deviations. False K-edge identification is possible in areas where the K-edge of the underlying element had a negligible impact on the recorded spectrum. Visible maxima in the derivation of the absorption coefficient were selected by the algorithm, leading to misinterpreted K-edges, and fluctuating assigned values. Incorrectly assigned values were filtered out. The filtering is based on the assumption that any absorption area is covering a detector area larger than one pixel.

The identification of overlapping elements is not possible with the technique presented. The dominating influence of a K-edge on the absorption spectrum will be only identified belonging to the element with the highest impact on the transmission spectrum. The detectability of the K-edges could be further increased by a better energy resolution of the detector. Changes in the transmission spectrum would have a higher impact, and elements could be assigned even more adequately. Additionally, the algorithm of K-edge assignment could be improved to allow multipeak identification. Higher statistics and proper noise-reduction analysis helps avoiding false peaks appearing in the derivatives. Beyond these limitations, the discussed method combined with the TPX3 detector has been successfully applied and demonstrated the possibility of the identification of several elements in a single X-ray image. Even chemical elements with a difference in the atomic number of 1 were assigned correctly within the uncertainty. Adjusting the detector-assembly and the energy spectrum could further improve the number of correctly detected pixels for use in different fields of applications. Elements with lower atomic numbers and K-edges in the lower energy range could be detected by combining the TPX3 detector with a Silicon sensor. The silicon sensor has the possibility to apply thresholds at lower energy due to its relatively noiseless operation and lower efficiency for higher X-ray energies.

The presented method has a strong potential in different fields of applications, e.g., the analysis of sectional biological samples of tumor tissue to determine a possible increased accumulation of one specific chemical. Highly efficient sensor materials, such as CdTe, enable the exploration of potential applications in fields like waste management and mining. The algorithm-based assignment of chemical elements also shows considerable potential for pixel-wise classification by applying machine learning (ML). It is envisioned that training ML models to identify the chemical elements by the transmission spectrum would improve the data analysis speed and make the element identification method practical. The application of element classification with ML algorithms will be further explored in future work.

References

[1] S. Singh and M. Singh, "Explosives detection systems (EDS) for aviation security," *Signal Process.*, vol. 83, no. 1, pp. 31–55, 2003, doi: 10.1016/S0165-1684(02)00391-2.

[2] S. U. Khan, I. U. Khan, I. Ullah, N. Saif, and I. Ullah, "A review of airport dual energy X-ray baggage inspection techniques: Image enhancement and noise reduction," *J. X-Ray Sci. Technol.*, vol. 28, no. 3, pp. 481–505, Jun. 2020, doi: 10.3233/xst-200663.

[3] G. E. M. Hall, G. F. Bonham-Carter, and A. Buchar, "Evaluation of portable X-ray fluorescence (pXRF) in exploration and mining: Phase 1, control reference materials," *Geochem., Explor., Environ., Anal.*, vol. 14, no. 2, pp. 99–123, May 2014, doi: 10.1144/geochem2013-241.

[4] S. P. Gundupalli, S. Hait, and A. Thakur, "A review on automated sorting of source-separated municipal solid waste for recycling," *Waste Manage.*, vol. 60, pp. 56–74, Feb. 2017, doi: 10.1016/j.wasman.2016.09.015.

[5] T. Su, V. Kaftandjian, P. Duvauchelle, and Y. Zhu, "Classification-based material decomposition method for photon counting-based spectral radiography: Application to plastic sorting," *Nucl. Instrum. Methods Phys. Res. A, Accel. Spectrom. Detect. Assoc. Equip.*, vol. 960, Apr. 2020, Art. no. 163537, doi: 10.1016/j.nima.2020.163537.

[6] R. E. Alvarez and A. Macovski, "Energy-selective reconstructions in X-ray computerised tomography," *Phys. Med. Biol.*, vol. 21, no. 5, pp. 733–744, Sep. 1976, doi: 10.1088/0031-9155/21/5/002.

[7] L. A. Lehmann et al., "Generalized image combinations in dual KVP digital radiography," *Med. Phys.*, vol. 8, no. 5, pp. 659–667, Sep. 1981, doi: 10.1118/1.595025.

[8] E. B. Hughes et al., "The angiography program at Stanford," *Nucl. Instrum. Methods Phys. Res. A, Accel. Spectrom. Detect. Assoc. Equip.*, vol. 246, nos. 1–3, pp. 719–725, 1986, doi: 10.1016/0168-9002(86)90179-8.

[9] V. L. Novikov, S. A. Ogorodnikov, and V. I. Petrunin, "Dual energy method of material recognition in high energy introscopy systems," *Issues At. Sci. Technol.*, vol. 35, no. 4, pp. 93–95, 1999. [Online]. Available: http://dspace.nbuv.gov.ua/handle/123456789/81505

[10] D. Vavrik and J. Jakubek, "Material analysis using characteristic transmission spectra," in *Proc. IEEE Nucl. Sci. Symp. Conf. Rec.*, Oct. 2008, pp. 2452–2455.

[11] X. Llopart, M. Campbell, D. S. Segundo, E. Pernigotti, and R. Dinapoli, "Medipix2—A 64 k pixel read out chip with 55 μm square elements working in single photon counting mode," in *Proc. IEEE Nucl. Sci. Symp. Conf. Rec.*, Nov. 2001, pp. 1484–1488.

[12] J. Rinkel et al., "Experimental evaluation of material identification methods with CdTe X-ray spectrometric detector," *IEEE Trans. Nucl. Sci.*, vol. 58, no. 5, pp. 2371–2377, Oct. 2011, doi: 10.1109/TNS.2011.2164266.

[13] J. Uher, J. Jakubek, S. Mayo, A. Stevenson, and J. Tickner, "X-ray beam hardening based material recognition in micro-imaging," *J. Instrum.*, vol. 6, no. 8, Aug. 2011, Art. no. P08015, doi: 10.1088/1748-0221/6/08/p08015.

[14] G. Beldjoudi, V. Rebuffel, L. Verger, V. Kaftandjian, and J. Rinkel, "An optimised method for material identification using a photon counting detector," *Nucl. Instrum. Methods Phys. Res. A, Accel. Spectrom. Detect. Assoc. Equip.*, vol. 663, no. 1, pp. 26–36, Jan. 2012, doi: 10.1016/j.nima.2011.09.002.

[15] A. Brambilla, A. Gorecki, A. Potop, C. Paulus, and L. Verger, "Basis material decomposition method for material discrimination with a new spectrometric X-ray imaging detector," *J. Instrum.*, vol. 12, no. 8, Aug. 2017, Art. no. P08014, doi: 10.1088/1748-0221/12/08/p08014.

[16] Z. Zhou et al., "Direct iterative basis image reconstruction based on MAP-EM algorithm for spectral CT," *J. Nondestruct. Eval.*, vol. 40, no. 1, pp. 1–10, Mar. 2021, doi: 10.1007/s10921-020-00736-8.

[17] M. Busi, J. Kehres, M. Khalil, and U. L. Olsen, "Effective atomic number and electron density determination using spectral X-ray CT," *Proc. SPIE*, vol. 10999, Apr. 2019, Art. no. 1099903. [Online]. Available: https://www.spiedigitallibrary.org/conference-proceedings-of-spie/10999/2519851/Effective-atomic-number-and-electron-density-determination-using-spectral-x/10.1117/12.2519851.full

[18] B. Xie et al., "Super-energy-resolution material decomposition for spectral photon-counting CT using pixel-wise learning," *IEEE Access*, vol. 9, pp. 168485–168495, 2021, doi: 10.1109/access.2021.3134636.

[19] Z. Zhang et al., "Experimental research of the energy bins for K-edge imaging using a photon counting detector: A phantom and mice study," *Radiat. Detection Technol. Methods*, vol. 4, no. 3, pp. 303–311, Sep. 2020, doi: 10.1007/s41605-020-00184-y.

[20] B. Xie et al., "ROI-wise material decomposition in spectral photon-counting CT," *IEEE Trans. Nucl. Sci.*, vol. 67, no. 6, pp. 1066–1075, Jun. 2020, doi: 10.1109/TNS.2020.2985071.

[21] B. Xie et al., "Material decomposition in X-ray spectral CT using multiple constraints in image domain," *J. Nondestruct. Eval.*, vol. 38, no. 1, p. 16, Mar. 2019, doi: 10.1007/s10921-018-0551-8.

[22] W. Wu, P. Chen, V. Vardhanabhuti, W. Wu, and H. Yu, "Improved material decomposition with a two-step regularization for spectral CT," 2019, *arXiv:1910.05259*.

[23] Z. Chen and L. Li, "Robust multimaterial decomposition of spectral CT using convolutional neural networks," *Opt. Eng.*, vol. 58, no. 1, Jan. 2019, Art. no. 013104, doi: 10.1117/1.oe.58.1.013104.

[24] S. Pani et al., "Optimization of K-edge subtraction imaging using a pixellated spectroscopic detector," in *Proc. IEEE Nucl. Sci. Symp. Med. Imag. Conf. Rec. (NSS/MIC)*, Anaheim, CA, USA, Oct. 2012, pp. 3063–3066.

[25] R. Ballabriga et al., "The Medipix3RX: A high resolution, zero dead-time pixel detector readout chip allowing spectroscopic imaging," *J. Instrum.*, vol. 8, no. 2, Feb. 2013, Art. no. C02016, doi: 10.1088/1748-0221/8/02/c02016.

[26] M. Schütz, S. Procz, J. Fey, and M. Fiederle, "Element discrimination via spectroscopic X-ray imaging with a CdTe Medipix3RX detector," *J. Instrum.*, vol. 15, no. 1, Jan. 2020, Art. no. P01006, doi: 10.1088/1748-0221/15/01/p01006.

[27] T. Poikela et al., "Timepix3: A 65 K channel hybrid pixel readout chip with simultaneous ToA/ToT and sparse readout," *J. Instrum.*, vol. 9, no. 5, May 2014, Art. no. C05013, doi: 10.1088/1748-0221/9/05/c05013.

[28] CERN. *Medipix3 Collaboration*. Accessed: Dec. 3, 2020. [Online]. Available: https://medipix.web.cern.ch/

[29] J. Jakubek, "Precise energy calibration of pixel detector working in time-over-threshold mode," *Nucl. Instrum. Methods Phys. Res. A, Accel. Spectrom. Detect. Assoc. Equip.*, vol. 633, pp. S262–S266, May 2011, doi: 10.1016/j.nima.2010.06.183.

[30] S. Procz, J. Lubke, A. Zwerger, M. Mix, and M. Fiederle, "Optimization of Medipix-2 threshold masks for spectroscopic X-ray imaging," *IEEE Trans. Nucl. Sci.*, vol. 56, no. 4, pp. 1795–1799, Aug. 2009, doi: 10.1109/TNS.2009.2025175.

[31] J. Fey, S. Procz, M. K. Schütz, and M. Fiederle, "Investigations on performance and spectroscopic capabilities of a 3 mm CdTe timepix detector," *Nucl. Instrum. Methods Phys. Res. A, Accel. Spectrom. Detect. Assoc. Equip.*, vol. 977, Oct. 2020, Art. no. 164308, doi: 10.1016/j.nima.2020.164308.

[32] M. C. Veale et al., "Measurements of charge sharing in small pixel CdTe detectors," *Nucl. Instrum. Methods Phys. Res. A, Accel. Spectrom. Detect. Assoc. Equip.*, vol. 767, pp. 218–226, Dec. 2014, doi: 10.1016/j.nima.2014.08.036.

[33] J. S. U. Parra et al., "Dose estimation in X-ray backscatter imaging with Timepix3 and TLD detectors," *J. Instrum.*, vol. 18, no. 5, May 2023, Art. no. P05042, doi: 10.1088/1748-0221/18/05/p05042.

[34] J. F. Hainfeld, D. N. Slatkin, T. M. Focella, and H. M. Smilowitz, "Gold nanoparticles: A new X-ray contrast agent," *Brit. J. Radiol.*, vol. 79, no. 939, pp. 248–253, Mar. 2006, doi: 10.1259/bjr/13169882.

[35] Bracco Imaging. *Kontrastmittel Für die Röntgendiagnostik*. Accessed: Jul. 5, 2022. [Online]. Available: https://imaging.bracco.com/de-de/produkte/kontrastmittel-f-r-die-r-ntgendiagnostik

[36] L. Tlustos et al., "Imaging properties of the Medipix2 system exploiting single and dual energy thresholds," *IEEE Trans. Nucl. Sci.*, vol. 53, no. 1, pp. 367–372, Feb. 2006, doi: 10.1109/TNS.2006.869844.

[37] J. Jakubek, A. Cejnarova, T. Holy, S. Pospisil, J. Uher, and Z. Vykydal, "Pixel detectors for imaging with heavy charged particles," *Nucl. Instrum. Methods Phys. Res. A, Accel. Spectrom. Detect. Assoc. Equip.*, vol. 591, no. 1, pp. 155–158, Jun. 2008, doi: 10.1016/j.nima.2008.03.091.

[38] L. Tlustos, M. Campbell, C. Fröjdh, P. Kostamo, and S. Nenonen, "Characterisation of an epitaxial GaAs/Medipix2 detector using fluorescence photons," *Nucl. Instrum. Methods Phys. Res. A, Accel. Spectrom. Detect. Assoc. Equip.*, vol. 591, no. 1, pp. 42–45, Jun. 2008, doi: 10.1016/j.nima.2008.03.020.

[39] NIST. *X-Ray and Gamma-Ray Data*. Accessed: Dec. 4, 2020. [Online]. Available: https://www.nist.gov/pml/x-ray-and-gamma-ray-data